Abnormal volume transport in the Banda Sea: a causal analysis by box model

Yiwei Zhang, Grant R. Bigg

Department of Geography, University of Sheffield, Sheffield, United Kingdom

Corresponding author: Yiwei Zhang (yzhang336@sheffield.ac.uk)

Key Points:

- Found a shift of transport stratification in the Banda Sea between depths of ~500 to 2700 m during 1993 to 2000.
- An ideal 3-layer box model has been used to simulate the Banda basin to test the model response for different upstream water sources.
- The shift could result from more water from the South Pacific entering the Banda Sea in layer 3 during 1993 to 1996.

Abstract

As one of the deepest basins over the Indonesian Seas, the Banda Sea is strongly involved in the thermohaline circulation component of the Indonesian Throughflow (ITF). Here, a shift of transport stratification in the Banda Sea has been found between depths of ~500 to 2700 m, with the vertical pattern of the transport changed from a two-component vertical structure of southward-northward during 1980 to 1992, to a three-component northward-southward-northward during 1993 to 2000. Therefore, the vertical distribution of the Banda Sea transport was then separated into three layers. To investigate possible reasons for this event, an ideal thermohaline circulation box model has been used to simulate the Banda basin. Extensive simulations are designed to test the model response for different upstream water sources. The results show that except for layer 1, the two deeper layers both show a prolonged effect after the cessation of changes to the input water sources. The results suggests the shift could result from a relatively short-term increase in the water source from the South China Sea or the South Pacific to layer 3, leading to an increase of southward transport. In layer 2, the model produced an increase in water flow to the north and vertically to both upper and lower layers. In the light of these model results, the reanalysis data was examined further – it is consistent with more water from the South Pacific entering the Banda Sea via the Lifamatola Strait in layer 3 during 1993 to 1996.

Plain Language Summary

We found a vertical transport structure shift happened during 1993 to 2000 at the Banda Sea. The purpose of this study is to investigate potential reason for this event by a simple physical ocean model. Comparing with other seas that the Indonesian Throughflow passing, the Banda Sea is one of few basin there which is able to involve thermohaline circulation. This means that a better understanding of transport vertical profile at the Banda Sea helps us to learn

the Pacific-Indian Ocean connection. Our results suggest that there was more water flowed into the Banda Sea from the South Pacific, which might link to the consisting El Niño events during that period. Future work should focus on the mechanism and theory of how ENSO influence on the water supply of the Indonesian Throughflow.

1 Introduction

As the only tropical connection between the Pacific and Indian Ocean, the Indonesian Throughflow (ITF) transports warm and salty water from the Pacific to the Indian Ocean and plays an essential role in the ocean heat and mass balance, and can significantly affect the thermohaline circulation, locally and remotely (Gordon 1986; Hirst and Godfrey 1993). The transport of the ITF shows strong seasonal and inter-annual variability, which are the results of monsoonal wind and ENSO (El Niño-Southern Oscillation) cycles (Miyama et al. 1995; Meyers 1996). The Pacific feeds the ITF mainly through the North and South Equatorial Current via the Makassar Strait and the Lifamatola Strait respectively (Gordon and Fine 1996; Valsala et al. 2010; Gordon 2011; Hu et al. 2015), and the South China Sea (SCS) indirectly transports Pacific water to the ITF via the Karimata Strait (Fig.1). Most of the inflow is achieved at the depth of the thermocline, although some enters deeper layers. However, due to the complicated bathymetry of the Indonesian Seas, the deeper circulation of this area is more complex but less understood. This research focuses on the Banda Sea which is one of the deepest sea basins among the Indonesian Seas. The Banda Sea is separated into two parts by a ridge: the North Banda basin reaches depths of ~5800 m, while the South Banda basin is about 5400 m deep. To the north, the Banda Sea connects the Maluku Sea via the Lifamatola Strait, and the Halmahera Sea via the Ceram Sea, through which inflows the relatively warmer and saltier South Pacific water (see Fig S1). As the second inflow passage, the Lifamatola Strait is controlled by a sill with a depth of 1940 m. To the southwest, the Banda Sea is next to the Flores Sea, which directly connects to the Makassar Strait, the biggest inflow passage of the ITF (Gordon and Susanto et al. 2003). Modelling results suggest that most water from the Makassar Strait enters the Banda Sea (Liang et al. 2019). Among all three main inflows of the ITF, the Makassar Strait is limited to the south by the Dewakang Sill of 680 m depth. Because of the depth of the Java Sea, the Karimata Strait only allows transport of Pacific water in a shallow layer. Therefore, the water deeper than ~680 m that is part of the Throughflow must enter the Indonesian Sea via the Lifamatola Strait and pass through the Banda Sea; for the outflow, water deeper than about 680 m is exported by the Timor Passage (Gordon and Giulivi et al. 2003). Thus, the Banda Sea plays a major role in the ITF.

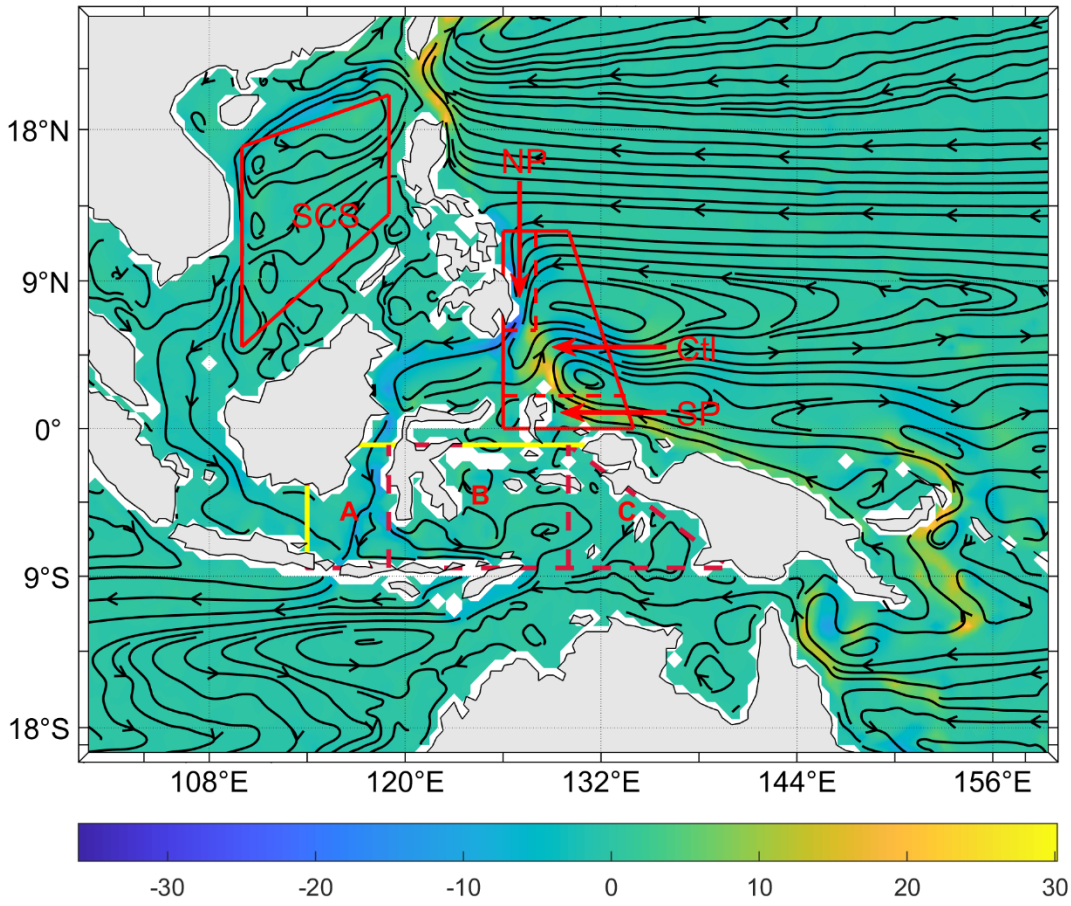

Figure. 1. The area of the Indonesian Seas. The solid lines indicate the ITF inflows calculation slices (Masumoto and Yamagata, 1993). Dashed box is the area averaged calculation region of the ITF transport, and is separated into 3 sub-region, as region A, B and C. The averaged area for the Pacific side boundary of Ctl, NP, SP and SCS runs for box model in red boxes (Part 3.2). The contour is the long term vertical averaged transport, unit: Sv; the streamlines indicate the current. See Fig. S1 for a map showing places and areas mentioned in this paper.

Current studies of the Banda Sea have focused on the surface water properties and transport (Zijlstra et al. 1990; Gordon and Susanto 2001; Horhoruw et al. 2017) and the tidal mixing (Castruccio et al. 2013). Like the rest of the Indonesian Seas, the Banda Sea transports waters to other basins or the Indian Ocean mostly at the upper layer but with energetic upwelling caused by the

Ekman pumping due to the monsoonal wind (Gordon and Susanto et al. 2003; Horhoruw et al. 2017). The upwelled water in the Banda Seas not only helps to well mix water from nearby basins and passages, but acts as a storage mechanism for the ITF (Gordon and Giulivi et al. 2003). Liang et al. (2019) found that the Banda Sea presents a clear three-layer pattern in an ocean model and by tracing the water sources, the composition of the water in the different layers was found to be different. In this paper, after first finding an observational shift of transport stratification in the Banda Sea, the influence of the different water sources on the vertical transport distribution is studied by using a simple physical box model.

2 The variability of the volume transport of the ITF, 1980-2015

Here, the Simple Ocean Data assimilation ocean/sea ice reanalysis (SODA 3.7.2) is used for investigating the hydrological properties of the ITF and Banda Sea. The ITF transport in each cell is defined by

$$\overrightarrow{q_u} = \vec{u} \times lat \times z; \quad (1)$$

$$\overrightarrow{q_v} = \vec{v} \times \text{lon} \times z; \quad (2)$$

$$q_{i,j,z} = \sqrt{\overrightarrow{q_u}^2 + \overrightarrow{q_v}^2}; \quad (3)$$

The $\vec{u}$ and $\vec{v}$ are the U and V component of the current velocity; the lon and lat are the step of the longitude and latitude. Because the ITF is generally a north-southward transport, the $q_{i,j,z}$ is multiplied by the zonal direction as $\overrightarrow{q_{i,j,z}}$, and area averaged over the dashed box shown in Fig.1. For the general ITF transport, the $q_{i,j,z}$ is calculated by different inflows, as the solid lines in Fig.1 shows. To unify the direction of inflows, the q_{Java} is multiplied by the horizontal direction, the q_{Makassar} and $q_{\text{Lifamatola}}$ are multiplied by the zonal direction. Therefore the whole ITF transport (Q_{ITF}) is determined by the sum of the transports of three inflows, as

$$Q_{\text{ITF}} = q_{\text{Makassar}} + q_{\text{Lifamatola}} + q_{\text{Java}} \quad (4)$$

As Fig. 2(a) shows, the average ITF transport by the SODA is -12.76 Sv. This can be compared with the mean INSTANT (Sprintall et al. 2009) transport of -15.07 Sv. The mean transport via the Makassar Strait from the MITF (Gordon et al. 2012) program is -10.52 Sv, -10.01 Sv, -8.63 Sv and -10.16 Sv respectively for the four periods monitored. In addition, a proxy calculated by satellite data (Susanto and Song, 2015) has an average ITF transport of -11.51 Sv. After processing all the MITF and proxy data, the correlations and t-tests with the ITF transport calculated here from SODA are listed in Table S2. The ITF transport is slightly smaller than the INSTANT in terms of its extreme values, but larger than MITF in general. For the proxy data, the ITF transport is stronger before 2000 but similar after.Generally comparing with all datasets here, the ITF transport calculated from SODA here is close in average with a clearly similar seasonal variation.

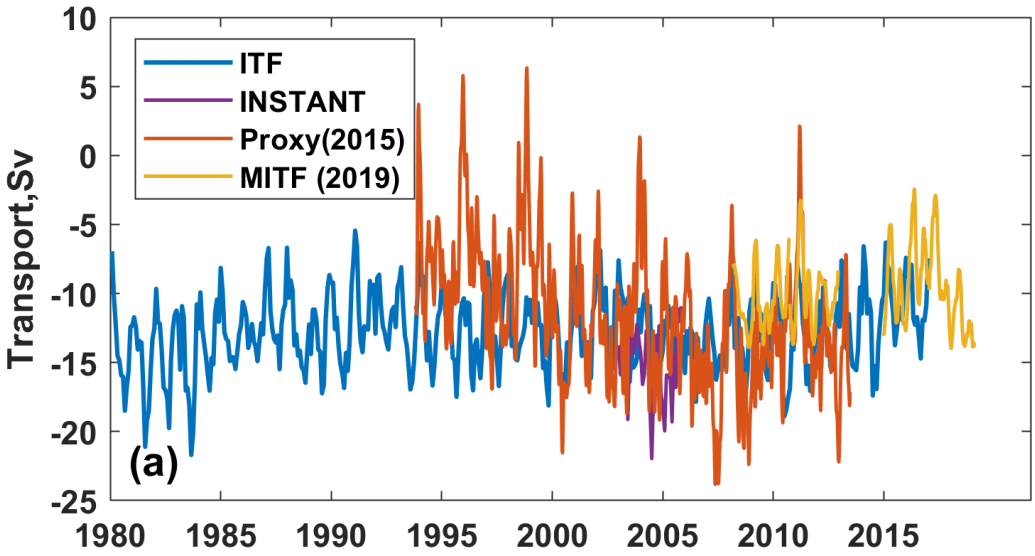

Figure. 2. (a)The monthly ITF transport variation (unit: Sv). The SODA reanalysis data in blue and the INSTANT data in purple, proxy data in orange and MITF data in yellow; (b) vertical distribution of the monthly averaged ITF transport anomaly during 1980 to 2016, unit: Sv; (c) The vertical distribution of transport over region B (see Fig. 1), unit: Sv. The transport anomaly is relative to the average of each SODA level. The positive value suggests northward transport anomaly. The dashed lines indicate different levels: top layer over depth range of surface to 330 m, middle layer over 330-~1500m and the deep layer over ~1500-2700 m.

In Fig. 2(b), the vertical profile of the ITF abnormal transport presents a clear shift over time. During 1980 to 1992, the upper layer (~500 to ~1500 m) presents a weak southward transport bias and the deep layer (~1500 to ~2500 m) has a significant northward transport bias. However, during 1993-2000, there is three-layer stratification as a strong northward-southward-northward transport anomaly occurs over this depth range. After 2000, the upper layer presents a complex northward transport bias but is more similar to what was observed in the first period. To understand the stratification of the abnormal transport we define layer 1 from the surface to 330m, layer 2 from 330m to ~1500m and layer 3 from ~1500m to ~2700m. To determine the physical origin of this shift in vertical profile during 1993 -2000, the ITF transport calculation region has been separated into 3 sub-regions (Fig.1) linked to the different main basins. The region B, which including the Banda Sea and Flores Sea, has the most similar vertical distribution (Fig.2(c)) to the overall ITF anomaly (see S3). Considering the depth of the vertical shift and sea basins, the Banda Sea is viewed as where the transport vertical shift was concentrated.

3 Modelling

3.1 Model description

The box model employed here is based on the idealized model for the thermohaline circulation developed by Stommel (1961). Fig. 3 shows the schematic diagram of the Banda Sea box model. For this model the Banda Sea is delimited by the box shown in Fig.3; the area of the box is 5.27×10^4 km^2, and the thickness of boxes 1, 2 and 3 are 330m, 1353m and 607.5m respectively, which are the same as the thicknesses of layers 1, 2 and 3 in Fig. 2. The water is assumed to be well mixed within each box, therefore all water properties are uniform in each box. The mass and energy are exchange by pipes which connect between boxes and with boundaries. The atmosphere-ocean interaction is simulated by the total freshwater and heat fluxes at the top surface of box 1. The thermohaline fluxes between the layers, denoted as $\mathbf{Q_{12}}$ and $\mathbf{Q_{23}}$, and those with the Pacific side boundary, $\mathbf{P_1}$, $\mathbf{P_2}$ and $\mathbf{P_3}$, and the Indian Ocean (IO) side, $\mathbf{I_1}$, $\mathbf{I_2}$ and $\mathbf{I_3}$, are driven by density differences.

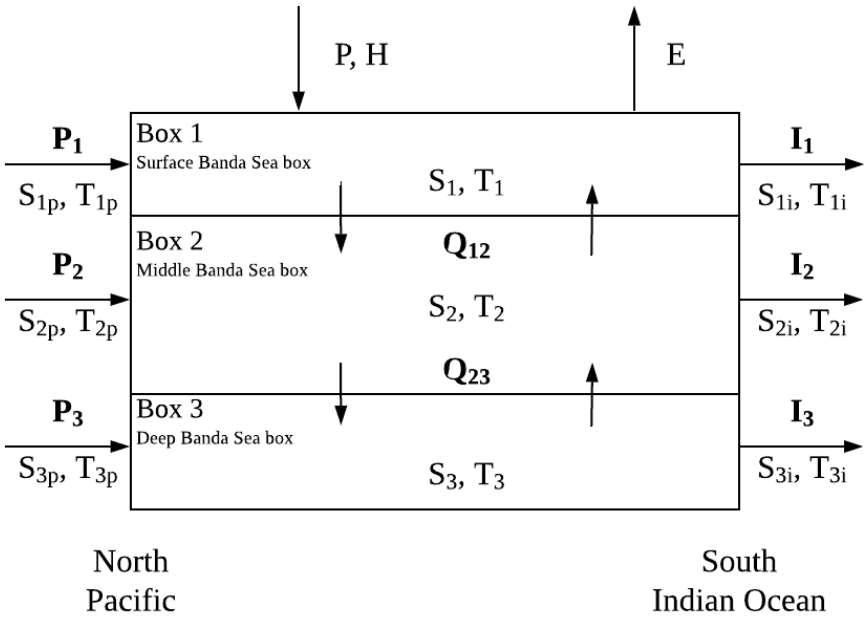

Figure. 3. The schematic diagram of the box model. The box 1, 2 and 3 indicate the layer 1, 2 and 3 in chapter 2; the P1 , P2 and P3 mean the inflow from the Pacific in different layers; I1, I2 and I3 mean the outflow to the Indian Ocean in different layers; Q12 and Q23 standard the vertical exchanged between box 1\2 and 2\3. All S and T represent the salinity and temperature fluxes, which exchanges with the current. The P is the precipitation and H is the heat flux with the atmosphere; E is the evaporation.

The advective fluxes Q_{nm} between boxes n and m, and P_n between the boxes n and the Pacific side boundary, are calculated as in Marotzke (2000):

$$Q_{\mathrm{nm}} = k_{\mathrm{nm}}[\alpha\,(T_n - T_m) - \beta(S_n - S_m)], \quad (4)$$

$$P_n = k_{\mathrm{xn}}\left[\alpha\,(T_p - T_n) - \beta\,(S_p - S_n)\right], \quad (5)$$

The T and S here mean the temperature and salinity of the boxes or side boundary input data (see Table 3); the thermal ( ) and saline ( ) expansion coefficients of seawater are listed in Table 1.

Table 1. Values of parameters used in the box model.

Parameters	Notation	Value
Thermal Expansion Coefficient	α	$1.5 \times 10^{-4}\ K^{-1}$
Saline Expansion Coefficient	β	8×10^{-4} psu^{-1}
Reference Seawater Density	ρ_o	$1026\ kg\ m^{-3}$
Heat Capacity of Seawater	$C_{p,o}$	$3990\ J$ kg^{-1} K^{-1}
Thermal Coupling Strength	λ	$35\ W\ m^{-2}\ K^{-1}$
Reference Salinity	S_r	$35\ psu$
Thermal Expansion Coefficient	α	$1.5 \times 10^{-4}\ K^{-1}$

The hydraulic constant (k) is a tuneable parameter which described all the dynamics of the thermohaline current (see values in Table 2). Based on (4) and (5), the theoretical hydraulic constants (k_t) for each flux, except I_n, are decided by,

$$k_{\mathrm{tnm}} = \frac{Q_{\mathrm{nm}}}{\alpha(T_m - T_n) - \beta(S_m - S_n)}, \quad (6)$$

Where the Q_{nm} here is the long-term averaged volume transport of each flux, listed in Table 2. To clarify, in Table 2, the fluxes from the Pacific are determined by the vertical sum of each box thickness of the north boundary of the Banda Sea basin instead of the full ITF itself, therefore the values of P_s are significantly smaller than the ITF volume transport. The T_n/T_m and S_n/S_m are the climatological mean temperature and salinity of box n/m or side boundaries (Table 3). All the k_t are listed in Table 2. The wind field and the Ekman effect play essential roles in the Banda Sea area (Gordon and Susanto 2001), but box 1 only interacts with the air by heat and freshwater fluxes exchange. On the other hand, the complicated topography of the Banda Sea makes the density gradient less important for the current in layer 3. Therefore, the k values should not only be decided by (6), but also need further adjustment to compensate for these additional effects, especially for fluxes related to box 3. Table 2 lists the adjusted k values used in the following simulations.

Table 2. The thermohaline flux properties.

Flux	Description of location	Value based on SODA (Sv)	Theoretical hydraulic constant, k_t (10
P_1	Box 1and Pacific side boundary	0.39885 (Southward)	2156.4916
P_2	Box 2 and Pacific side boundary	0.2283(Northward)	11698.0939
P_3	Box 3 and Pacific side boundary	0.3142(Southward)	2782.0081
Q_{12}	Box 1 and 2	0.0186 (upward)	7.75
Q_{23}	Box 2 and 3	0.0935 (upward)	149.691

All advective exchanges calculated in this way are scalar quantities. The directions of these exchanges are determined by the density difference. Here, a simplified linear density calculation is utilized, as,

$\rho = \rho_0(1 - \alpha T + \beta S)$, (7)

where the ρ_0 is reference seawater density (see Table 1). The transport between boxes and the Indian Ocean side boundary is calculated by each box mass balance, as

$I_1 = P_1 - Q_{12} + \mathrm{FW}^C$, (8)

$I_2 = P_2 + Q_{12} - Q_{23}$, (9)

$I_3 = P_3 + Q_{23}$, (10)

The long-term climatological averaged freshwater flux (FW^C) is averaged across 1980 to 2016.

Based on the NCEP/NCAR (National Centers for Environmental Prediction – National Center for Atmospheric Research) reanalysis 1 (Kalnay et al. 1996), the climatological downward surface heat fluxes (Q_1^c) of box 1 is calculated by the sum of the latent heat (LH), sensible heat (SH), net longwave radiation (NL) and net shortwave radiation (NS), as,

$Q_1^c = NS - (LH + SH + NL)$. (11)

From the Haney type boundary (Haney 1971), under the Newtonian cooling law, the modelled reservoir heat flux of the box 1 (Q_1^m) would be:

$Q_1^m = \lambda(T_1^* - T_1^m)$, (12)

where is the thermal coupling strength (Table 1), T_1^m is the modelled box 1 temperature and T_1^* is the prescribed apparent temperature of box 1, defined as,

$T_1^* = T_1^c + \frac{Q_1^c}{\lambda}$, (13)

The long-term climatological averaged temperature of box 1, T_1^c is calculated from the SODA data. The box 1 restoring time constant ( ) is related to , as:

$\tau = \frac{C}{\lambda} = \frac{C_{p,o}\rho_o D_1}{\lambda}$, (14)

where C is the heat capacity per unit area, $C_{p,o}$ is the specific heat capacity of seawater (Gill 1982), and ρ_o is a reference density of seawater (Table 1). The D_1 is the depth of box 1. Therefore (12) can be written as:

$$Q_1^m = \frac{C_p \rho_o D_1}{\tau}(T_1^* - T_1^m), \quad (15)$$

Thus the modelled heat flux of box 1, $H_{T_1}^m$, is

$$H_{T_1}^m = Q_1^m \times A_1 = \frac{C_p \rho_o D_1 A_1}{\tau}(T_1^* - T_1^m) = \frac{C_p M_1}{\tau}(T_1^* - T_1^m), \quad (16)$$

The A_1 and M_1 represent the area and mass of water respectively in box 1. Therefore, the rate of temperature change in box 1 due to atmosphere-ocean exchange is represented by

$$\frac{\partial T_1^m}{\partial t} = \frac{1}{\tau}(T_1^* - T_1^m) = \frac{H_{T_1}^m}{C_p M_1}, \quad (17)$$

For box n, the rate of change of the temperature caused by exchanges with side boundary m or box m, is calculated by,

$$\frac{\partial T_n^m}{\partial t} = \frac{|Q_{\mathrm{mn}}|(T_m - T_n)}{V_m}, \quad (18)$$

The Q_{mn} and T_m are the transport between box n and side boundary (box) m and temperature of side boundary (box) respectively. Thus the time rate of temperature change for box 1 is given as:

$$\frac{\partial T_1^m}{\partial t} = \frac{H_{T_1}^m}{C_p M_1} + \frac{|Q_{1m}|(T_m - T_1)}{V_1}, \quad (19)$$

Similarly, the box 1 salinity is decided by both mass exchanges and surface freshwater fluxes. The surface freshwater flux depends on the evaporation (E), precipitation (P) and runoff. However, there is no major river on the islands surrounding the Banda Sea. Thus, the surface freshwater flux for box 1 with area A_1 used here is,

$$FW = (E - P) \times A_1, \quad (20)$$

Therefore the "virtual" salinity flux (Kahana et al. 2004) is employed here, H_S^C,

$$H_S^C = S_r \times \frac{\mathrm{FW}^C}{V_1}, \quad (21)$$

where S_r is the reference salinity, 35 psu. Utilizing the similar Newtonian restoring law on the box 1 salinity with the same time parameters in (14), the modelling restoring salinity of box 1 can be written as

$$H_{S_1}^m = \frac{1}{\tau}(S_1^* - S_1^m), \quad (22)$$

where the prescribed apparent salinity, S_1^*, is calculated:

$$S_1^* = S_1^C + \frac{\mathrm{FW}^C \times S_r}{V_1} \times \tau = S_1^c + H_{S_1}^C \times \tau, \quad (23)$$

Here the S_1^C is the climatological salinity of the box 1, calculated by the SODA dataset. Therefore, the time rate of change for salinity in box 1, due to air-sea exchange is:

$\frac{\partial S_1^m}{\partial t} = \frac{1}{\tau}(S_1^* - S_1^m) = H_{S_1}^m$, (24)

In addition, the rate of salinity change caused by the exchange between box n with side boundaries m and/or box 2, can be calculated as:

$\frac{\partial S_n^m}{\partial t} = \frac{|Q_{\mathrm{nm}}|(S_m - S_n)}{V_n}$, (25)

Therefore, the time rate of salinity change for box 1 is:

$\frac{\partial S_1^m}{\partial t} = H_{S_1}^m + \frac{|Q_{1m}|(S_m - S_1)}{V_1}$, (26)

In the box model, the temperature and salinity of box 1 are calculated using (16) and (23), and of box 2/3 using (18) and (25). The equations are solved by the Runge-Kutta 4th order method.

3.2 The experimental plan for the box model (including the purpose of experiments and the input data source)

The experiments are designed in two groups: a control run and sensitivity runs. Each experiment is run for 30 years, every simulating year is 365 days, and the time step is 100 seconds. For the control run (Ctl run), the Pacific side boundary input data, P_1, P_2 and P_3 (see Fig.3), are area averaged as shown in Fig.1. This area includes both the Mindanao Current and the New Guinea Coastal Current (NGCC) but does not include water from the South China Sea. The sensitivity runs are designed to test the effects of different water sources on the Banda Sea. Thus, the sensitivity runs are constructed with 3 options: the North Pacific run (NP), the South Pacific run (SP) and the South China Sea run (SCS). In this way, instead of changing the ratio of inflow water source structure, the sensitivity runs adjust the side boundary input to be composed of just one pure source. The Pacific side boundary input data for all the sensitivity runs are area averaged as indicated in Fig 1. The temperature and salinity of all the runs are listed in Table 3. In sensitivity runs, the first 5 years of each simulation used the Ctl run side boundary input data, but during the 6th to 15h year, the Pacific side boundary input data is replaced by different pure sources. From the 16th year, the side boundary input changes back to the Ctl run format.

Table 3. The temperatures and salinities of the Pacific side boundary input in all runs.

Parameters	Runs	$\mathbf{T_{P1}}$(℃)	$\mathbf{T_{P2}}$(℃)	$\mathbf{T_{P3}}$(℃)	$\mathbf{S_{P1}}$(psu)	$\mathbf{S_{P2}}$(psu)	$\mathbf{S_{P3}}$(psu)
Values	Ctl	21.6549	5.7138	1.9966	34.5561	34.5552	34.639
Entry 2, 1	NP	22.0138	5.5870	1.9856	34.5351	34.509	34.6378
	SP	22.4817	6.1059	2.0368	34.6486	34.6001	34.6419
	SCS	20.0584	6.1300	2.3181	34.2160	34.5025	34.6178

4 Box model results

4.1 Contol simulation result

The modelled temperature, salinity and transport of the Ctl run are presented in Fig 4. They are fairly stable, with only a slight drift in the properties of box 3. The average modelled temperature for box 1, 2 and 3 are 21.26 ℃, 6.04 ℃ and 2.37℃ respectively, consistent with the long-term climatological temperatures based on the SODA dataset (see Table 4). The mean simulated salinity for each box are 34.3 psu, 34.6 psu and 34.62 psu respectively; these also agree with the climatological salinity over the Banda Sea. For the transport, it is to be noted that, unlike the SODA dataset, the direction of the transport is counter-geographical for horizontal transport, with southward transport being positive and northward transport negative. In the case of vertical transport, downwards is positive and upwards is negative. For the Pacific side boundary input fluxes, the value of the P_1, P_2 and P_3 are 0.32 Sv, -0.01 Sv and 0.032 Sv, all consistent with Table 2; the Q_{12} and Q_{23} in the Ctl run are -0.0196 Sv and -0.0663 Sv so upward in both boxes; for the outflow fluxes, I_1, I_2 and I_3 are 0.77 Sv, -0.037 Sv and -0.063 Sv respectively, so there is only outflow to the Indian Ocean from box 1 and weak inflow from the other two boxes. Except for P_3, the Ctl run successfully simulated all fluxes (comparing with Table 2). Because the Lifamatola Strait is in reality shallower than the depth of box 3, the water is well mixed before entering the Banda Sea, which is not included in the box model. Generally, however, the box model is considered to successfully simulate the horizontal transport in each box. In the Ctl run, box 1 fluxes reached equilibrium within the first 3 years. The horizontal flow is the main process in each box. Due to the relatively small vertical fluxes (Q_{12} and Q_{23}), the inflow from the Pacific and the outflow to the IO are close to each other in all three boxes. For box 2, the P_2 and I_2 present a strengthening trend in northward transport, the P_2 and I_2 increased from ~-0.02 Sv and 0.02 Sv to ~0 Sv and ~0.05 Sv respectively. In box 3, the P_3 shows a stable trend but the I_3 and Q_{23} decreased from ~-0.057Sv and ~-0.06 Sv to ~-0.07 Sv both during 30 years simulation. The behaviour of box 2 and 3 might not be ideal, but acceptable as a simple physical basin model.

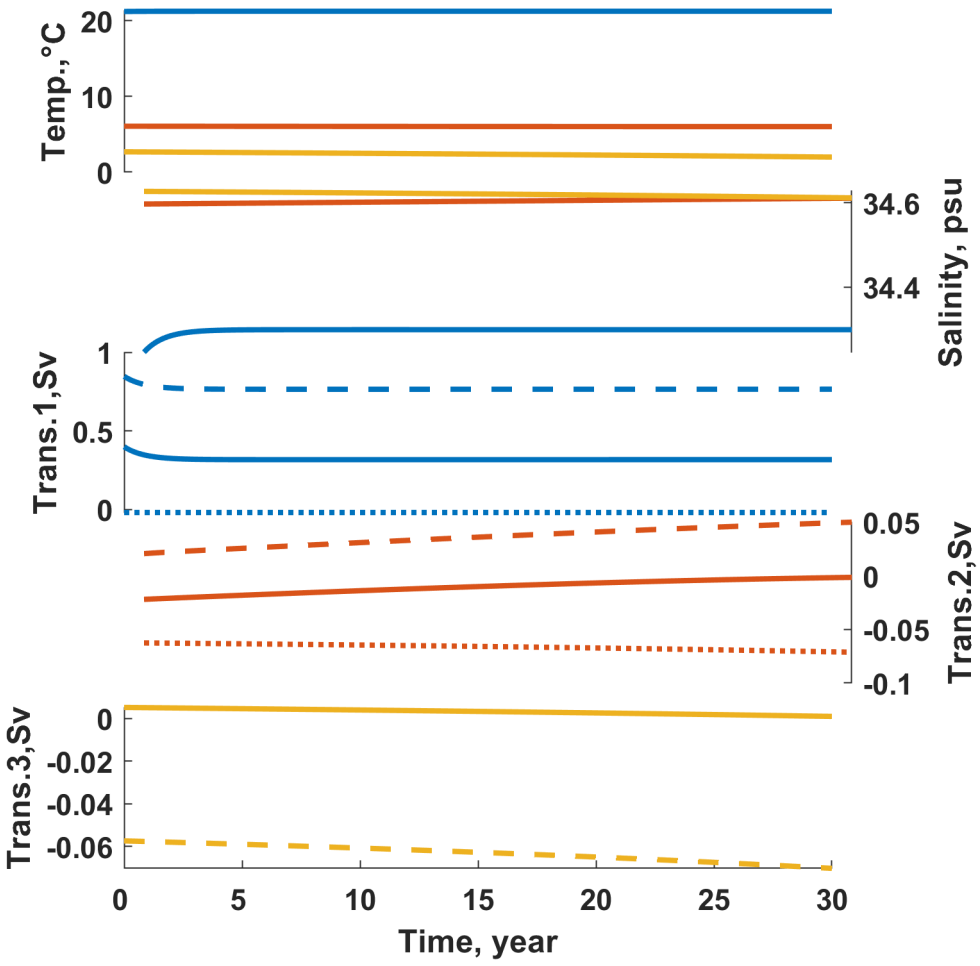

Figure 4. The modelled temperature, salinity and transport of the Ctl run. Blue means box 1, red means box 2 and yellow means box 3. For the transport series, P_s in solid line, I_s in dashed line and, Q_{12} and Q_{23} in dotted line. For the P_s and I_s, the southward transport is in positive, and the northward transport in negative; for vertical transport, Q_{12} and Q_{23}, the positive value means downward transport, and the negative means upward transport. The sign of the transport value representatives the same direction in following this paper.

Table 4. The water properties of each box from the SODA dataset and Ctl run.

Data	T_1, ℃	T_2, ℃	T_3, ℃	S_1, psu	S_2, psu	S_3, psu
SODA	21.23	6.07	2.69	34.24	34.60	34.63

Data	T_1, ℃	T_2, ℃	T_3, ℃	S_1, psu	S_2, psu	S_3, psu
Ctl	21.26	6.04	2.37	34.30	34.60	34.62

4.2 Sensitive simulation results

The sensitivity runs examining different water sources are next compared (see Table 3 for input T and S). For box 1, the difference of temperature, salinity and transport between the Ctl run and the sensitivity runs are presented in Fig 5. After the input into the Pacific side boundary changes in year 5, all sensitivity experiments tend to decrease the Banda Sea temperature in layer 1.The North Pacific water cools box 1 the most, by $\sim 6.87 \times 10^{-4}$ ℃, the South Pacific the second most and the SCS water cools box 1 down about half the strength of the NP run, but all of the temperature anomalies changed back to near zero after the perturbation stopped. The average temperature anomalies during and after the perturbation (year 6 to 15) are listed in Table 5. In the case of salinity variation, all sensitive runs present a freshening effect on box 1, the NP decreased the salinity by about 0.012 psu, the SP decreased about 0.008 psu and about 0.005 for the SCS, in 5 years and reached balance before the anomalous input ends. Similar to the case for temperature, the disturbance to salinity trends tends to disappear after year 15 rapidly, and reach balance again at about year 20. The overall box 1 abnormal transport present a negative bias for all sensitivity runs, the lowest values happening immediately the anomaly started, reaching -0.3 Sv, -0.22 Sv and -0.14 Sv, for the NP, SP and SCS runs respectively . These levels are then maintained throughout the inputting period. The maximum transport anomalies appear when the

imposed anomaly ceases, and the anomalies reach equilibrium within three years.

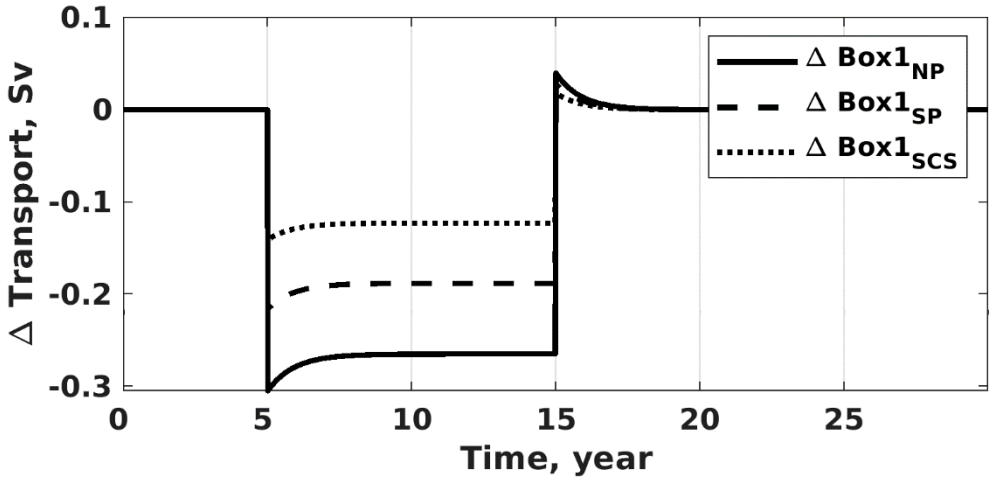

Figure 5. The anomaly of temperature, salinity and transport between the Ctl run and sensitive runs in box 1.

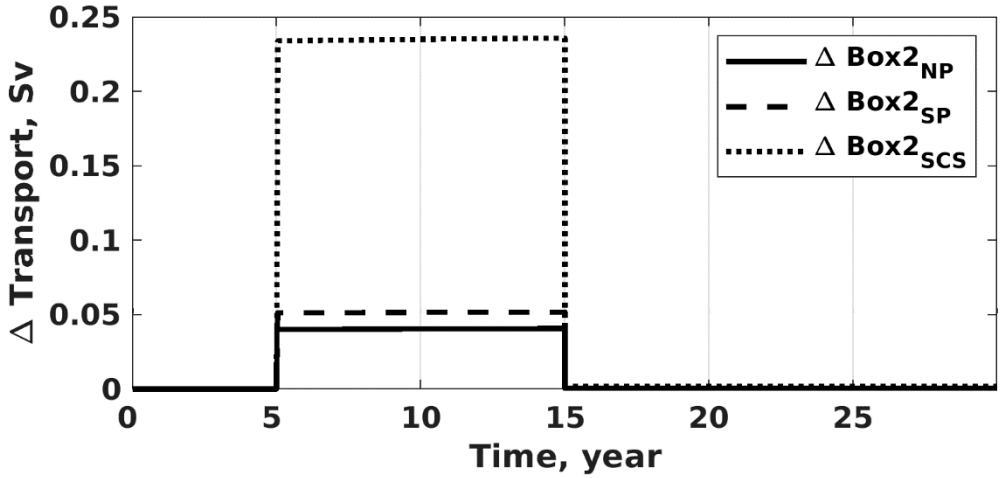

Figure 6. The abnormal temperature, salinity and transport between the Ctl run and sensitive runs in the box 2.

In box 2 (Fig 6), all three runs warm the Banda Sea to a greater extent than is the case for box 1. Unlike in box 1, this temperature variation continued throughout years 6 to 15 and had only a slight cooling tendency after the imposed input anomaly ceased after year 15. At the end of year 15, the temperature anomalies reached a maximum as 1.65×10^{-4} ℃, 4.66×10^{-4} ℃ and 0.0032 ℃ for the NP, SP and SCS runs respectively. After the perturbation was removed, all the temperature anomalies decreased with time but remained high at the end of simulation. For salinity variation, the SCS water supplement increased the box 2 salinity about 0.0017 psu during the perturbation with this being only slightly decreased to 0.0016 psu by the end of the simulation; the NP and SP runs presented a similar increasing pattern but to smaller values, 4.05×10^{-4} psu and 4.59×10^{-4} psu at the end of the perturbation, and remained at similar values at the end of simulation. The average temperature and salinity anomalies during and after

the perturbation are listed in Table 5. With respect to the transport, the replacement of the input with SCS water decreased the transport significantly, by approximately 0.24 Sv, during the disturbance (P_2 = -0.01 Sv in Ctl run); the NP and SP runs also show a decreasing effect on box 2 transport, but of less than a quarter the size of that in the SCS run. After changing the input data back to the Ctl plan, the anomalous transport of the NP, SP and SCS runs reduced to close to 0 Sv immediately.

In Fig 7, the sensitivity results for box 3 are shown. The deviations of tem-

perature are positive for all the runs. The abnormal temperature between the Ctl and SCS is much bigger than the anomalies with NP and SP inputs. For the SCS run, the rate of increase became slower after the disturbance input ceased but remaining positive, and reached a maximum when the simulation ended. All sensitivity tests showed continued temperature rise in box 3 after the anomaly was removed. For salinity, the SCS water freshened box 3 the most comparing with the other 2 runs, the freshening anomaly reaching 4.44×10^{-4} psu by the end of the run. The South Pacific run freshened box 3 also, but by less (minimum: -2.77×10^{-5} psu). The North Pacific water increased the salinity in box 3, marginally, by about 2.69×10^{-6} psu at the maximum. When the Pacific side input data switched back to the Ctl plan, all salinity differences kept their tendency and arrived at their maximum at the end of the simulations. The box 3 temperature and salinity differences of the Ctl run compared to the sensitivity runs are shown in Table 5. Fig. 11 also shows the horizontal transport responses of the sensitivity runs. For the horizontal transport, the SCS run presented a strong northward transport bias, the peak appeared at the beginning of perturbation (~ -0.0059 Sv), reduced only slightly during the perturbation period (to -0.0057 Sv). After the perturbation ceased transport changed to a slight southward bias ($\sim 2.83 \times 10^{-4}$ Sv). The SP run showed a slight northward transport anomaly during the imposition of the anomaly, with this almost returning to Ctl values after the input anomaly ceased. In the case of the NP water experiment box 3 transport saw slightly more water moving to the south (7.43×10^{-5} Sv averagely) during the anomaly phase, and this tendency remained after the anomaly ceased ($\sim \sim \ 4.11 \times 10^{-5}$ Sv).

Fig 8 shows the vertical transport difference of Q_{12} and Q_{23} between the Ctl and sensitivity runs. For Q_{12}, all three sensitivity runs trend to strengthen the upward transport. During the anomalous input stage, all three runs increased the transport quickly during the first 3 years, but with the rate of increase slowing thereafter. These increasing trends stopped immediately after the anomalies ceased, decreasing over about 3 years but then remaining slightly negative for the rest of the simulation. For Q_{23}, unlike the Q_{12}, all three anomalies are positive which mean these sensitivity runs weakened the upward transport. During the inputting period, the NP and SP show a small weakening bias; the SCS run decreased the Q_{23} most with a stronger trend. After the inputting ends, all three variations maintained the upward bias, but with a much slower increasing rate.

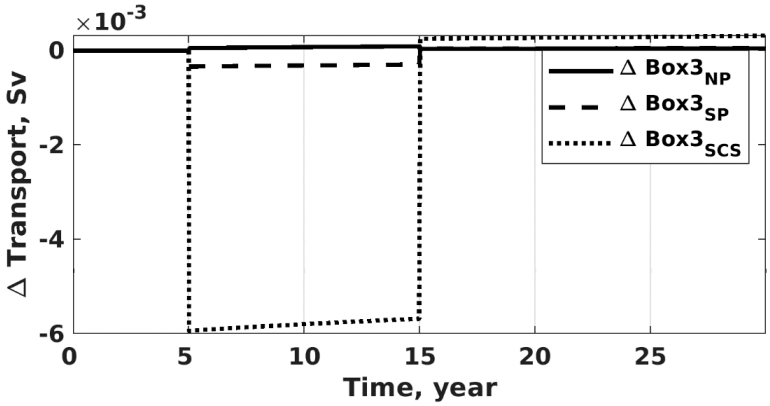

Figure 7. The abnormal temperature, salinity and transport between the Ctl run and sensitive runs in the box 3.

Table 5. The temperature and salinity anomaly between the Ctl and sensitive runs of boxes during and after perturbation inputting.

Parameters	NP	SP	CSC
Mean T_1 (yr 6-15; 10^{-4} ℃)	-6.35	-4.46	-2.85
Mean T_1 (yr $>$ 15; 10^{-5} ℃)	-1.98	-1.34	-0.28
Mean S_1 (yr 6-15; psu)	-0.01	-0.01	-0.01
Mean S_1 (yr $>$ 15; 10^{-4} psu)	-6.72	-4.71	-3.08
Mean T_2 (yr 6-15; 10^{-5} ℃)	7.2720	20.9880	146.6111
Mean T_2 (yr $>$ 15; 10^{-5}℃)	7.0018	37.8670	287.2037
Mean S_2 (yr 6-15; 10^{-4} psu)	2.0693	2.3761	9.3372
Mean S_2 (yr $>$ 15; 10^{-4} psu)	4.0477	4.5101	16.9984
Mean T_3 (yr 6-15; 10^{-5} ℃)	0.62	9.29	138.03
Mean T_3 (yr $>$ 15; 10^{-4} ℃)	1.45	3.21	33.81
Mean S_3 (yr 6-15; 10^{-5} psu)	0.14	-1.05	-17.97
Mean S_3 (yr $>$ 15; 10^{-5} psu)	0.21	-2.48	-40.70

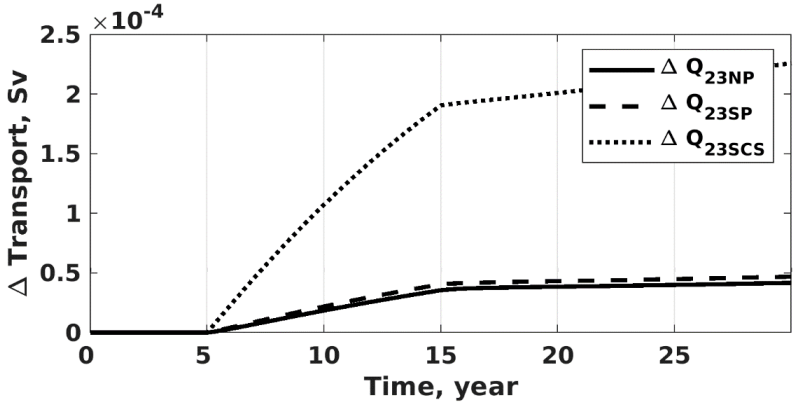

Figure 8. The abnormal vertical transport between the Ctl run and sensitive runs, unit: Sv.

5 Discussion

For the Ctl results, the simulation is reasonably realistic. The layer 1 transport reached equilibrium within the first 3 years and maintained this throughout the simulation. However, in box 2, the P_2 and I_2 roughly stabilized in the first 10 years but continued strengthening afterwards. Moreover, in box 3, the P_3 and I_3 present a negative flux trend during the whole simulation. The reason for the unstable variation in boxes 2 and 3 might be because the box volume is too small comparing with the strong input fluxes. On the other hand, the Banda Sea is highly affected by Ekman pumping (Potemra 1999; Gordon and Susanto 2001; Horhoruw et al. 2017). However, the box model only allows the ocean to interact with the atmosphere by freshwater and heat fluxes exchange. Without a proper wind field applied to box 1, it is impossible for the box model to simulate the Ekman pumping effectively. Thus, the vertical transport between boxes was simulated poorly.

Comparing the box model sensitivity run results with Figs. 2(b) and 2(c), the possible reason for the transport vertical shift during 1993 to 2000 might be that there was a relatively short surge from the SCS or the South Pacific to the Banda Sea into layer 3. Therefore, after this surge, layer 3 had more water transported to the south and in layer 2, not only was there more water transport to the north, but also more water flowed vertically into this layer from both layers 1 and 3. The Mindoro Strait connects the South China Sea and the Sulu Sea. Although, the South China Sea supplies the Banda Sea through both the Karimata Strait and the Mindoro Strait, the depth of the Java Sea limits its ability to directly supply the deep transport Thus, the Mindoro Strait represents the effective transport from the South China Sea to the Banda Sea, the Lifamatola Strait provides the South Pacific water source route and the Makassar Strait that for the North Pacific water (see Fig. S1 for locations). Fig 9 presents the SODA annual transport variance via the Mindoro Strait, the Lifamatola Strait, and

the Makassar Strait in layer 3. In 1993, the Mindoro Strait fed more water into layer 3, but this was short-lived. In the case of the Lifamatola Strait, more water flowed into the Banda Sea during the whole of 1993 to 2000. Although, the box model results suggest that the box 3 transport is more sensitive to the SCS perturbation, the Ctl run water source is composed of a mixture of the North and South Pacific water, which naturally suggests the observed behavior would be closer to the NP and SP sensitivity runs. Therefore, more water flowing into the deep Banda Sea during 1993 to 2000 from the South Pacific is most likely to be the cause of the Banda Sea's vertical distribution shift in transport found in section 2. The reason for there being more water coming from the South Pacific might be related to the persistent El Niño events during the decade.

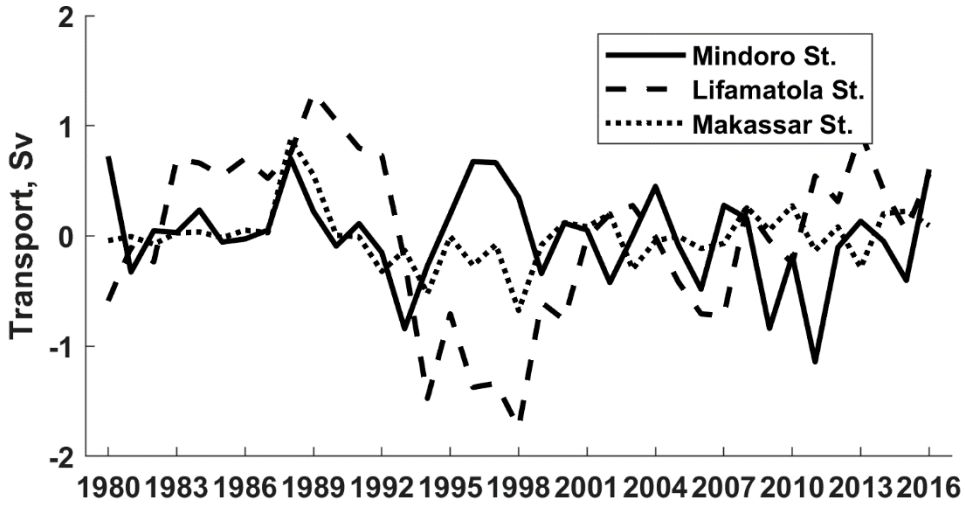

Figure 9. The annual transport variance series via the Mindoro Strait, the Lifamatola Strait, and the Makassar Strait in layer 3, unit: Sv.

Acknowledgments

We acknowledge Dr.Susanto for his kind help and all data providers.

Open Research

The SODA data used for transport calculation and initialising the box model in the study are available at NOAA via https://www2.atmos.umd.edu/~ocean/ with free access (Carton et al. 2018). The INSTANT data used in part 2 in the study are available at CSIRO via https://www2.atmos.umd.edu/~ocean/ with login access (Sprintall et al. 2009). The MITF data used in part 2 in the study are available at University of Columbia via http://ocp.ldeo.columbia.edu/res/div/ocp/projects/MITF/Makassar_Strait_Mooring.html with free access (Gordon et al. 2012). The proxy data used in part 2 in the study also are kindly provided by Dr. Susanto (Susanto and Song 2015). The NECP/NCAR reanalysis 1 dataset used for initialising the box model are available at NOAA

via https://psl.noaa.gov/data/gridded/data.ncep.reanalysis.html with free access (Kalnay et al. 1996).

R2020a of the MATLAB used for all coding and plotting work, including the box model is preserved at https://uk.mathworks.com/products/new_products/release2020a.html, available via individual/organization license and developed openly at https://uk.mathworks.com/products/matlab.html . The ETOPO1 data used in support information are available at NCAR via https://rda.ucar.edu/datasets/ds759.4/index.html with free access (NGDC, 2011).

References

Carton, J. A., Chepurin, G. A., & Chen, L. (2018). SODA3: A new ocean climate reanalysis. Journal of Climate, 31(17), 6967–6983. https://doi.org/10.1175/JCLI-D-17-0149.1

Castruccio, F. S., Curchitser, E. N., & Kleypas, J. A. (2013). A model for quantifying oceanic transport and mesoscale variability in the Coral Triangle of the Indonesian/Philippines Archipelago. Journal of Geophysical Research: Oceans, 118(11), 6123–6144. https://doi.org/10.1002/2013JC009196

Gill, Adrian E. Atmosphere-ocean Dynamics. New York ; London: Academic, 1982. Print. International Geophysics Ser. ; 601pp.

Gordon, A. L. & Fine, R. (1996). Pathways of water between the Pacific and Indian oceans in the Indonesian seas. Nature. 379. 146-149. 10.1038/379146a0.

Gordon, A. L., & Susanto, R. D. (2001). Banda Sea surface-layer divergence. Ocean Dynamics, 52(1), 2–10. https://doi.org/10.1007/s10236-001-8172-6

Gordon, A. L., Giulivi, C. F., & Ilahude, A. G. (2003). Deep topographic barriers within the Indonesian seas. Deep-Sea Research Part II: Topical Studies in Oceanography, 50(12–13), 2205–2228. https://doi.org/10.1016/S0967-0645(03)00053-5

Gordon, A. L., Susanto, R. D., & Vranes, K. (2003). Cool Indonesian throughflow as a consequence of restricted surface layer flow. Nature, 425, 824. Retrieved from https://doi.org/10.1038/nature02038

Gordon, A. L. (2011). Oceanography of the Indonesian Seas. Oceanography, 18(4), 13–13. https://doi.org/10.5670/oceanog.2005.18

Gordon, A. L., Huber, B. A., Metzger, E. J., Susanto, R. D., Hurlburt, H. E., & Adi, T. R. (2012). South China Sea throughflow impact on the Indonesian throughflow. *Geophysical Research Letters*, *39*(11), 1–7. https://doi.org/10.1029/2012GL052021

Horhoruw, S. M., Atmadipoera, A. S., Nanlohy, P., & Nurjaya, I. W. (2017). Anomaly of surface circulation and Ekman transport in Banda Sea during "Normal" and ENSO episode (2008-2011). IOP Conference Series: Earth and Environmental Science, 54(1), 12041. https://doi.org/10.1088/1755-1315/54/1/012041

Hu, D., Wu, L., Cai, W., Gupta, A. Sen, Ganachaud, A., Qiu, B., … Kessler, W. S. (2015). Pacific western boundary currents and their roles in climate. Nature. https://doi.org/10.1038/nature14504

Kahana, R., Bigg, G. R., & Wadley, M. R. (2004). Global ocean circulation modes derived from a multiple box model. Journal of Physical Oceanography, 34(8), 1811–1823. https://doi.org/10.1175/1520-0485(2004)034<1811:GOCMDF>2.0.CO;2

Kane, S. N., Mishra, A., & Dutta, A. K. (2016). Anomaly of surface circulation and Ekman transport in Banda Sea during "Normal" and ENSO episode (2008-2011). Journal of Physics: Conference Series, 755(1). https://doi.org/10.1088/1742-6596/755/1/011001

Liang, L., Xue, H., & Shu, Y. (2019). The Indonesian Throughflow and the Circulation in the Banda Sea: A Modeling Study. Journal of Geophysical Research: Oceans, 124(5), 3089–3106. https://doi.org/10.1029/2018JC014926

Masumoto, Y., & Yamagata, T. (1993). Simulated seasonal circulation in the Indonesian Seas. Journal of Geophysical Research, 98(C7), 12501. https://doi.org/10.1029/93JC01025

National Geophysical Data Center/NESDIS/NOAA/U.S. Department of Commerce (2011), ETOPO1, Global 1 Arc-minute Ocean Depth and Land Elevation from the US National Geophysical Data Center (NGDC), https://doi.org/10.5065/D69Z92Z5, Research Data Archive at the National Center for Atmospheric Research, Computational and Information Systems Laboratory, Boulder, Colo. Accessed 18 Jan 2019.

Potemra, J. T. (1999). Seasonal variations of upper ocean transport from the Pacific to the Indian Ocean via Indonesian Straits. Journal of Physical Oceanography, 29(11), 2930–2944. https://doi.org/10.1175/1520-0485(1999)029<2930:SVOUOT>2.0.CO;2

Sprintall, J., Wijffels, S. E., Molcard, R., & Jaya, I. (2009). Direct estimates of the indonesian throughflow entering the indian ocean: 2004-2006. Journal of Geophysical Research: Oceans, 114(7), 1–19. https://doi.org/10.1029/2008JC005257

Susanto, R. D., and Song, Y. T. (2015), Indonesian throughflow proxy from satellite altimeters and gravimeters, J. Geophys. Res. Oceans, 120, 2844– 2855, doi:10.1002/2014JC010382.

Valsala, V., Maksyutov, S., & Murtugudde, R. (2010). Possible interannual to interdecadal variabilities of the Indonesian throughflow water pathways in the Indian Ocean. Journal of Geophysical Research: Oceans, 115(10), 1921–1940. https://doi.org/10.1029/2009JC005735

Zijlstra, J. J., Baars, M. A., Tijssen, S. B., Wetsteyn, F. J., Witte, J. I., Ilahude, A. G., & Hadikusumah. (1990). Monsoonal effects on the hydrography of the upper waters (<300 M) of the eastern Banda Sea and northern Arafura Sea,

with special reference to vertical transport processes. Netherlands Journal of Sea Research, 25(4), 431–447. https://doi.org/10.1016/0077-7579(90)90068-R